



Effect of Tempering on the Ductile-to-Brittle Transitional Behavior of Ni-Cr-Mo Low-Alloy Steel

F.W. DelRio¹ · M.L. Martin¹ · R.L. Santoyo¹ · E. Lucon¹

Received: 5 March 2020 / Accepted: 1 July 2020 / Published online: 13 July 2020

© This is a U.S. government work and not under copyright protection in the U.S.; foreign copyright protection may apply 2020

Abstract

Background About 10 years ago, super-high energy Charpy specimens at the National Institute of Standards and Technology were removed from inventory due to unacceptable variability in absorbed energy, leading to the advent of new methods and materials to reduce the variability and maintain the prescribed energy levels.

Objective In this paper, we investigated the ductile-to-brittle transitional behavior of Ni-Cr-Mo low-alloy steel by testing Charpy specimens with side-grooves as a function of the final temper temperature to define the processing conditions for these super-high energy levels.

Methods For each temper, absorbed energy and force-displacement data were measured as a function of test temperature; the former was used to assess transition temperature and upper-shelf energy and the latter was used to estimate shear fracture appearance (*SFA*).

Results From the upper-shelf energy results, it was found that two of the temper conditions yielded energies in the super-high energy range and that side-grooves reduced the variability of the energy by preventing the formation of shear lips. From the *SFA* data, it was shown that the instrumented striker data and fractography were in excellent agreement, with the minor discrepancies attributed to difficulties with transitional fracture surfaces in the fractography and multiple crack arrest points in the instrumented striker data.

Conclusions In all, the data provided clear evidence that Ni-Cr-Mo low-alloy steel is a good solution for super-high energy Charpy indirect verification specimens.

Keywords Ductile-to-brittle transition · Shear fracture appearance · Impact test · Low-alloy steel · Charpy

Introduction

For the last 35 years, the National Institute of Standards and Technology (NIST) has developed standard reference materials, technologies, and processes for Charpy impact testing, which is utilized worldwide to ensure the reliability and safety of structural elements in infrastructure. NIST provides certification to a traceable measurement system via indirect verification specimens at three absorbed energy levels: low energy (13 J to 20 J), high energy (88 J to 136 J), and super-high energy (176 J to 244 J) [1]. About ten years ago, the super-high energy specimens were removed from inventory due to

unacceptable variability in the absorbed energy, leading NIST researchers to explore new methods and materials to (1) reduce the variability and (2) maintain the prescribed energy levels. Lucon [2] showed that both (1) and (2) could be achieved via changes to *both* specimen geometry and material type—the variability was reduced via 10% side-grooves in the specimens and the energy levels were maintained through a switch to a Ni-Cr-Mo low-alloy (AISI 9310) steel. In this paper, we investigated the ductile-to-brittle transitional behavior of AISI 9310 steel by testing Charpy specimens with side-grooves as a function of the final temper temperature to define the processing conditions for super-high energy levels. For each temper, absorbed energy and force-displacement data were collected at various test temperatures to assess the transition temperature and upper-shelf energy and estimate shear fracture appearance, respectively. The upper-shelf energies were compared to those needed for super-high energy levels and shear fracture appearance estimates were compared to those measured from scanning electron microscopy, thus

✉ F.W. DelRio
frank.delrio@nist.gov

¹ Applied Chemicals and Materials Division, Material Measurement Laboratory, National Institute of Standards and Technology, Boulder, CO 80305, USA



providing a quantitative method to assess the suitability of AISI 9310 steel as a traceable artifact for the verification of high-toughness steels in infrastructure.

Experimental Methods

AISI 9310 (AMS 6265) steel was produced from a single heat to minimize compositional and microstructural variations. The primary melt was prepared in an arc furnace, transferred to an argon-oxygen decarburization vessel for refining, bottom poured into electrodes, and vacuum-arc remelted into 76.2 cm ingots. The ingots were press forged at 1093 °C into 12.7 cm billets and rolled into 6 cm diameter bars. The round bars were cut into six equal lengths, heated to 1093 °C for final rolling to 13 mm square bars, cooled to room temperature, and cut into lengths of ≈ 1.7 m. The square bars were annealed in a vacuum furnace with oil-integrated quenching via the following scheme: normalization process, neutral-hardening process, deep-freeze cycle, and final-temper process. In this work, the final temper temperature T_f was varied, such that the bars were exposed to no final temper, 510 °C, 543 °C, and 566 °C. The bars were cut and ground into Charpy specimens with nominal dimensions of 55 mm \times 10 mm \times 10 mm, each with a 2-mm deep notch perpendicular to the longitudinal axis [1] and two side-grooves for a total thickness reduction of 1 mm, or 10% [2]. The orientation of all specimens was the same with respect to the initial 13 mm square bars.

The chemical composition was characterized using combustion, X-ray fluorescence, or optical emission spectroscopy. The microstructure was examined via electron backscatter diffraction (EBSD) in a scanning electron microscope (SEM) at 30 kV. The specimens were cut, mounted, and polished, such that the out-of-plane direction was parallel to the sample long axis. 200 $\mu\text{m} \times 200 \mu\text{m}$ images with 0.5 μm steps were taken, and routine clean-up was performed using neighbor confidence index correlation to reduce noise. The absorbed energy KV transition curves were obtained by testing 25 specimens at temperatures T from -196 °C to 21 °C (KV is the commonly-used designation for the energy absorbed by fracturing a V-notched Charpy specimen). KV curves were fit to an asymmetric hyperbolic tangent model

$$KV = A + B \tanh [(T - T_0)/(C + DT)], \quad (1)$$

where A , B , C , D , and T_0 were fixed or variable parameters [3]. Here, A and B were fixed; the upper-shelf energy USE and lower-shelf energy LSE were taken as the average KV values from each region and used to find A and B by $A = (USE + LSE)/2$ and $B = (USE - LSE)/2$. In contrast, C , D , and the transition temperature T_0 were variable, and evaluated by non-linear least-squares curve fitting to the data with a Levenberg-Marquardt iteration algorithm. Force F -

displacement d curves were collected with an instrumented striker statically calibrated in a universal testing machine. The F - d curves were studied to assess several key parameters, which were related to shear fracture appearance SFA by

$$SFA = 100 [1 - (F_{bf} - F_a) / (F_m + k(F_m - F_{gy}))], \quad (2)$$

where F_{gy} is the general yield force, F_m is the maximum force, F_{bf} is the unstable fracture force, F_a is the arrest force, and $k = 0.5$ [4]. SFA was also measured in an SEM at 30 kV. The ductile areas of fracture were determined based on the topography and size of the features, in addition to more subtle indicators such as depth of the feature and presence of river lines.

Results and Discussion

The weight percent of each element in the AISI 9310 steel is shown in Table 1. Two samples were examined, the first at the top of an ingot and the second at the bottom of an ingot. As shown in the table, the results from the two samples were in good agreement, suggesting that the chemical composition of the ingot was invariant across its length. In addition, the results from both samples were compared to the compositional requirements of AMS 6265P with the exceptions: $\text{Cu} \leq 0.20$, $P \leq 0.010$, $S \leq 0.010$, $V \leq 0.030$, $\text{Nb} \leq 0.005$, and $\text{Ti} \leq 0.003$. As shown in the table, both samples fell within the prescribed limits, even with the more stringent requirements for Cu, P, and S and added requirements for V, Nb, and Ti (used to reduce variability in the microstructure and absorbed energy). The EBSD images at each T_f are shown in Fig. 1. The grain size, or packet size, given the martensitic nature of this steel, was $\approx 3 \mu\text{m}$. Also, the orientation texture was largely invariant with T_f . Kozmel et al. [5] and Dong et al. [6] described similar grain sizes for heat-treated AISI 9310 steel. The former study showed the average grain size was between 1 μm and 8 μm and depended on temperature, strain, and strain rate, while the latter study described μm -sized grains with a smallest grain size of 1.2 μm .

The KV data and asymmetric hyperbolic tangent fits are shown in Fig. 2(a). For all T_f , the data and fits are in good agreement, indicating that the ductile-to-brittle behavior of the AISI 9310 steel is well described by equation (1). The fitting parameters for the model are given in Table 2. As expected, $USE = A + B$ increased as T_f increased, likely due to the amount of martensite tempering during the different heat treatments. Interestingly, the relationship between T_0 and T_f was non-monotonic; T_0 initially increased and then decreased as T_f increased. The latter trend is in good agreement with work on low-energy, high-energy, and super-high energy specimens [7]. The F - d data for specimens in the brittle ($T = -196$ °C), transitional ($T = -60$ °C), and ductile ($T = 22$ °C) regions of the $T_f = 543$ °C data set are shown in Fig. 2(b). The



Table 1 Chemical composition in weight percent as determined from combustion, X-ray fluorescence, and optical emission spectroscopy. The results were compared to the compositional requirements of AMS 6265P with the following exceptions: maximum limits were reduced for Cu, P,

and S and added for V, Nb, and Ti. Samples 1 and 2 were taken from the top and bottom of an ingot, respectively. The remaining weight percent is Fe

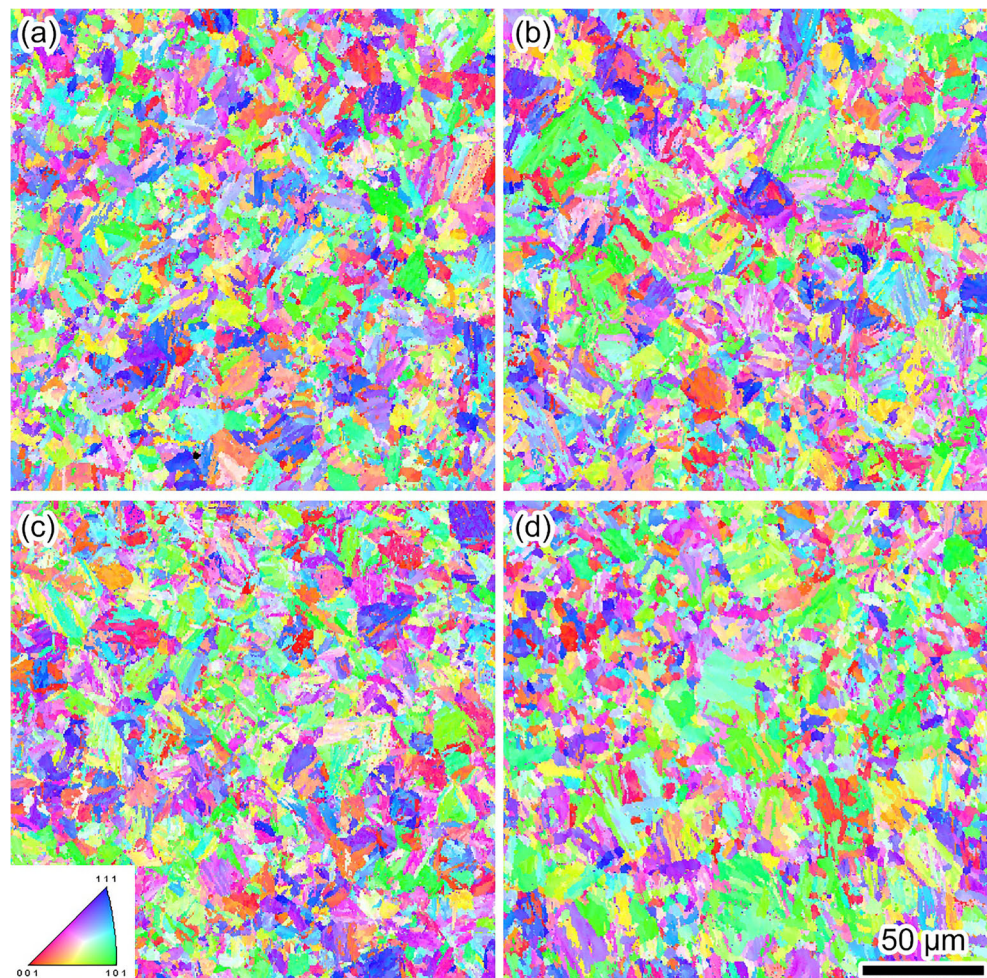
	Ni	Cr	Mn	Si	Mo	C	B	Cu	P	S	V	Nb	Ti
Min	3.00	1.00	0.40	0.15	0.08	0.07	–	–	–	–	–	–	–
1	3.35	1.30	0.49	0.33	0.13	0.12	<0.001	0.10	0.006	0.001	0.003	<0.005	0.002
2	3.30	1.29	0.56	0.32	0.12	0.10	<0.001	0.09	0.006	0.001	0.003	<0.005	0.002
Max	3.50	1.40	0.70	0.35	0.15	0.13	0.001	0.20	0.010	0.010	0.030	0.005	0.003

instrumented data in Fig. 2(b) were taken from the circled points in Fig. 2(a). In the brittle curve, the elastic section transitioned instantly to unstable crack propagation, such that $F_{gy} = F_m = F_{bf}$ and $F_a = 0$. In the transitional curve, the force increased up the elastic region through yielding to the maximum force and then decreased via stable and unstable crack propagation, leading to distinct values of F_{gy} , F_m , F_{bf} , and F_a . In the ductile curve, only stable crack propagation occurred, such that F_{bf} and F_a are undefined. Therefore, it was found that *SFA* increased from 0% to 100% as T increased from

–196 °C to 21 °C per equation (2), with the exact values in the transition region dependent on T and T_f .

The fracture surfaces and their respective *SFAs* were evaluated by SEM as shown in Fig. 3. A low-magnification image of an example fracture surface is shown in Fig. 3(a). The notch is at the top of the image. At the outset, only a large pocket on the left side and a few smaller pockets throughout the remainder of the surface were clearly designated as ductile failure at this scale. However, this only translated to an *SFA* of $\approx 10\%$, while the data from the F - d curve suggested an *SFA* closer to

Fig. 1 EBSD images of specimens with (a) no final temper, (b) $T_f = 510$ °C, (c) $T_f = 543$ °C, and (d) $T_f = 566$ °C. For all final temper conditions, the average grain size or packet size was ≈ 3 μm with minimal changes in the orientation texture with T_f



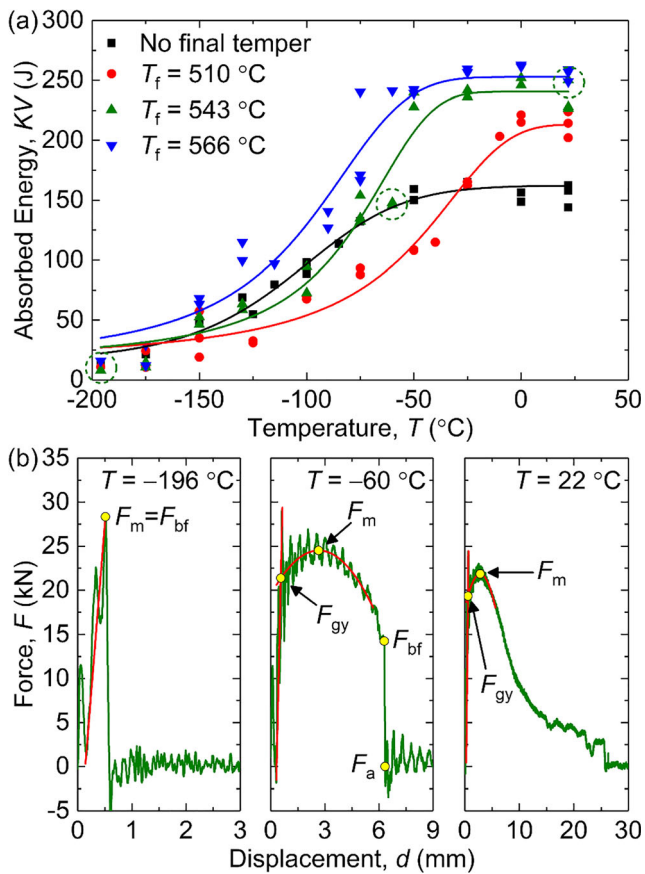


Fig. 2 (a) KV data for specimens with no final temper, $T_f = 510$ °C, $T_f = 543$ °C, and $T_f = 566$ °C. The KV values were fit to an asymmetric hyperbolic tangent model to assess the transition temperature and upper-shelf energy. (b) F - d data for specimens in the brittle ($T = -196$ °C), transitional ($T = -60$ °C), and ductile ($T = 22$ °C) regions for $T_f = 543$ °C; the instrumented striker data in (b) correspond to the circled points in (a)

42%. A closer examination of the fracture surfaces implied a more complicated story, though. Several higher-magnification images of other fracture surfaces are given in Fig. 3(b) to (d). Figure 3(b) shows an area dominated by cleavage fracture, where different planes of brittle failure were joined by small steps of ductile dimples (highlighted). Figure 3(d) illustrates a single cleavage facet (highlighted) surrounded by ductile dimples. Figure 3(c) shows a transitional state where areas of

cleavage and dimples were mixed, with the divisions between regions highlighted. These three states, and the multitude of intermediate mixtures, were often found on a single sample. As such, sampling of small areas of a fracture surface may not provide a representative view, for example, missing the large pocket of ductile failure in Fig. 3(a), leading to inaccurate measurements of SFA . To ensure accurate measurements, a tiled montage of higher-magnification images was taken for each surface. Ductile and brittle regions were identified and SFA was calculated using image processing software. As before, it was found that SFA increased from 0% to 100% as T increased from -196 °C to 21 °C, with the values dependent on T and T_f .

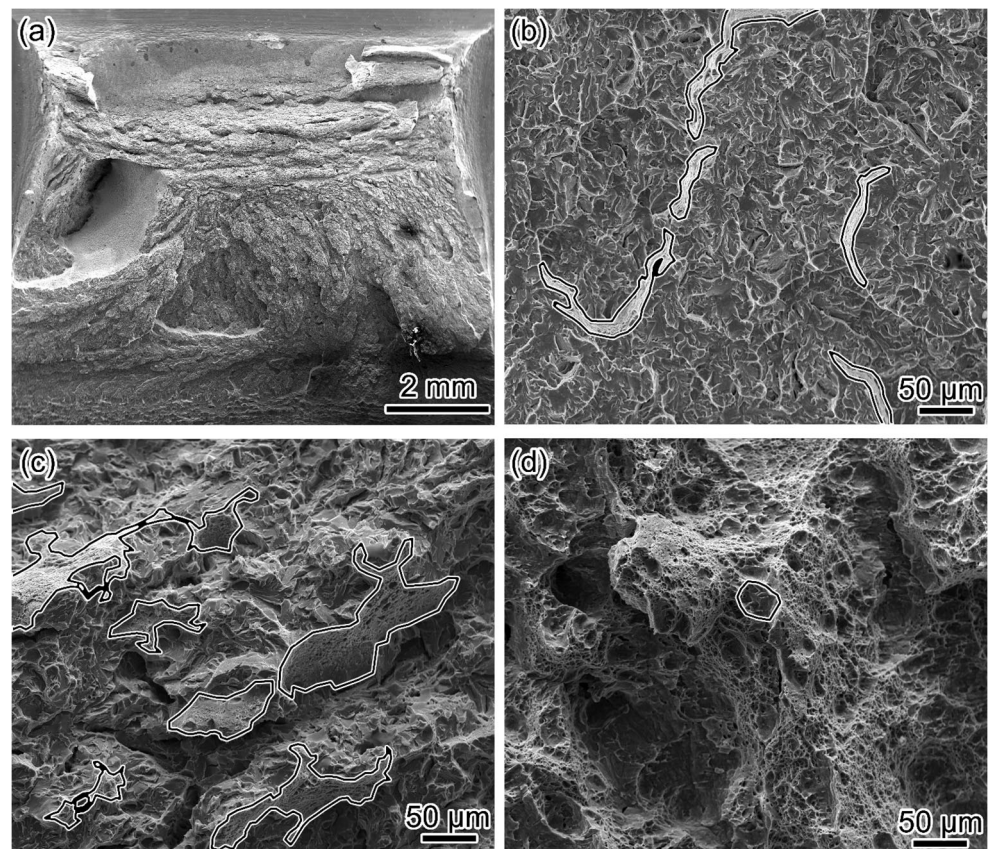
The SFA results from instrumented striker data and fractography of eight specimens are shown in Fig. 4. The solid line signifies perfect agreement between the results, while the dashed lines denote the errors typically observed for most materials as defined in ASTM E2298 and ISO 14556. Overall, the results suggest good agreement between the two methods (i.e., all data points fall within the 20% uncertainty bounds). Notably, the point with the largest difference exhibited an SFA of $\approx 60\%$ to 80% . Manahan et al. [8] proposed that fractographic SFA in the 55% to 80% range tend to exhibit more scatter for two reasons: (1) uncertainty in the determination method and (2) uncertainty in the operator interpretation. The determination method used here (i.e., capture a digital image and measure the SFA via image processing software) has the lowest uncertainty of the methods described in ASTM E23. As such, the discrepancy may be from operator interpretation of the fracture surfaces. McCowan et al. [9] offered an alternative reason for the difference based on a systematic study of nine steels with different absorbed energies. The authors found that high-energy 4340 steel exhibited a finely-spaced mixture of ductile and brittle regions, resulting in a distinct crack arrest point and an unambiguous determination of F_a . In contrast, super-high energy API X70 steel revealed distinct fracture features, leading to multiple arrest points and uncertainty in F_a . In that work, it was suggested that AISI 9310 steel falls into the latter category. Thus, the discrepancies in Fig. 4 could also be the result of operator interpretation of the instrumented data.

Table 2 Fitting parameters for the asymmetric hyperbolic tangent model to the KV transition curves. A and B were fixed and determined from the average KV in the upper-shelf and lower-shelf regions, while C , D , and T_0 were variable and evaluated by non-linear least-squares curve

T_f (°C)	A (J)	B (J)	C (°C)	D	T_0 (°C)
–	88.1 ± 4.2	74.1 ± 4.2	39.5 ± 23.0	-0.12 ± 0.20	-106.1 ± 4.8
510	112.0 ± 9.0	101.3 ± 9.0	30.5 ± 16.2	-0.46 ± 0.22	-50.5 ± 6.4
543	125.8 ± 12.7	114.8 ± 12.7	11.7 ± 27.8	-0.41 ± 0.30	-78.4 ± 6.4
566	132.4 ± 9.0	120.4 ± 9.0	17.7 ± 38.2	-0.35 ± 0.34	-98.8 ± 8.8

fitting to the data. Uncertainty values represent two standard deviations from multiple measurements (A and B) or a 95% confidence level in the fit (C , D , and T_0)

Fig. 3 (a) Low-magnification image of a fracture surface. At this scale, only a large pocket on the left side and a few smaller pockets throughout the remainder of the surface were clearly designated as ductile failure. Higher-magnification images of fracture surfaces with (b) mostly brittle, (c) mixed, and (d) mostly ductile regions. Here, the brittle and ductile regions were more obvious, making a tiled montage of such images a more accurate method for the determination of the global *SFA*



It is important to evaluate the absorbed energy and shear fracture appearance results as metrics to the suitability of AISI 9310 steel as a super-high energy Charpy standard reference material. From Fig. 2(a), it is evident that $USE = 213.3$ J at $T_f = 510$ °C and $USE = 240.6$ J at $T_f = 543$ °C, indicating that both final temper conditions yielded energies in the super-high energy range (176 J to 244 J). In addition, it was shown in previous work that 10% side-grooves reduced the variability of the absorbed energy by preventing the formation of shear lips, such that the variability fell within the acceptable limits

with only a 10% decrease in energy [2]. In contrast, T200 specimens demonstrated a similar decrease in variability with 10% side-grooves, but with a 30% decrease in energy. As a result, AISI 9310 steel specimens are more apt to retain the required energy levels. From Fig. 4, *SFA* from the instrumented striker data and fractography are in excellent agreement, thereby validating equation (2) as an acceptable alternative to fractography. The discrepancies in the ductile-to-brittle transition are due to difficulties associated with transitional fracture surfaces in the fractography and multiple crack arrest points in the instrumented striker data.

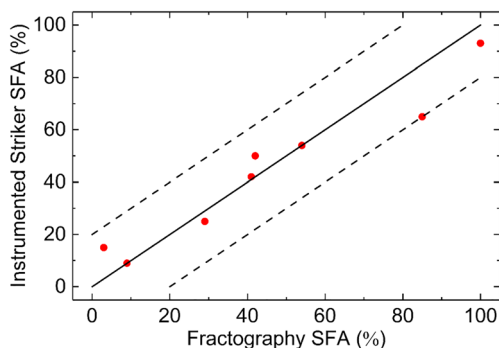


Fig. 4 Comparison of *SFA* from instrumented striker data and global fractographic measurements. The solid line represents a perfect correlation between the two measurements, while the dashed lines represent a $\pm 20\%$ difference as stipulated in ASTM E2298 and ISO 14456

Conclusions

In summary, we studied the absorbed energy and shear fracture appearance of AISI 9310 steel Charpy specimens with 10% side-grooves as a function of the final temper conditions. For all T_f , the absorbed energy data and asymmetric hyperbolic tangent fits were in good agreement, indicating that the ductile-to-brittle transitional behavior is well described by equation (1). *SFA* from instrumented data and fractography were also in agreement, thereby validating equation (2) as an acceptable alternative to fractography. In all, the data provided clear evidence that AISI 9310 steel is a good solution for super-high energy Charpy indirect verification specimens.

Acknowledgments Contribution of the National Institute of Standards and Technology, an agency of the US government; not subject to copyright in the USA.

Compliance with Ethical Standards

Conflict of Interest The authors declare that they have no conflict of interest.

References

1. McCowan CN, Siewert TA, Vigliotti DP (2003) The NIST Charpy v-notch verification program: overview and operating procedures. In: McCowan CN, Siewert TA, Vigliotti DP (eds) Charpy verification program: reports covering 1989–2002, NIST technical note 1500–9. National Institute of Standards and Technology, Gaithersburg, pp 3–42
2. Lucon E (2019) Influence of shear lip symmetry on the fracture behavior of Charpy specimens. *J Test Eval* 47:1129–1146
3. Helm JL (1996) The interpretation of Charpy impact test data using hyper-logistic fitting functions. In: Gelles DS, Nanstad RK, Kumar AS, Little EA (eds) Effects of radiation on materials: 17th international symposium, ASTM STP 1270, American Society for Testing and Materials, pp. 363–374
4. Chaouadi R, Fabry A (2002) On the utilization of the instrumented Charpy impact test for characterizing the flow and fracture behavior of reactor pressure vessel steels. *Eur Struct Integr Soc* 30:103–117
5. Kozmel T, Chen EY, Chen CC, Tin S (2014) Kinetics of sub-micron grain size refinement in 9310 steel. *Metall Mater Trans A* 45A:2590–2600
6. Dong M, Cui X, Lu B, Feng X, Song S, Jin G, Wang H (2020) Influence of surface nanocrystallization pretreatment on high-temperature vacuum carburizing behavior. *J Mater Process Technol* 278:116519
7. Lucon E, McCowan CN, Santoyo RL (2015) Impact characterization of 4340 and T200 steels by means of standard, sub-size and miniaturized Charpy specimens. *NIST Tech Note* 1858:1–58
8. Manahan MP, McCowan CN, Manahan MP (2008) Precent shear area determination in Charpy impact testing. *J ASTM Int* 5:1–15
9. McCowan CN, Lucon E, Santoyo RL (2019) Fracture appearance of steels in transition: experimental observations and measurements. *J Test Eval* 47:1009–1022

Publisher's Note Springer Nature remains neutral with regard to jurisdictional claims in published maps and institutional affiliations.

